Simulation Modelling Practice and Theory 16.9 (2008): 1438–1452

DOI: http://dx.doi.org/10.1016/j.simpat.2008.08.002

CEST and MEST: Tools for the Simulation of Radio Frequency Electric Discharges in Waveguides

Francisco Pérez[1*], Juan de Lara[1], Luis Conde[2],
Manuel Alfonseca[1], Luis Galán[3], David Raboso[4]

[1]Polytechnic School, Universidad Autonóma de Madrid, Spain
[2]Physics Dep., ETSI Aeronáuticos, Universidad Politécnica de Madrid, Spain
[3]Dep. of Applied Physics, Universidad Autónoma de Madrid, Spain
[4]European Space Agency/ESTEC, Noordwijk, The Netherlands

Abstract

In this paper we present two software tools for the simulation of electron multiplication processes in radio frequency (RF) waveguides. The electric discharges are caused by the multiplication of a small initial number of electrons. These are accelerated by the RF field and produce new electrons either by collisions with the walls of the waveguide (ripping new electrons from them), or by ionization of the neutral atoms of a gas inside the device.

MEST allows simulating the *Multipactor* effect, a discharge produced in vacuum and generated by the collision of the electrons with the walls. CEST simulates the discharge when in addition a neutral gas is present in the waveguide, at pressures lower than ground levels (often denominated *Corona* discharge). The main characteristic of both tools is that they implement individual-based, microscopic models, where every electron is individually represented and tracked. In the case of MEST, the simulation is discrete-event, as the trajectory of each electron can be computed analytically. In CEST we use a hybrid simulation approach. The trajectory of each electron is governed by the Langevin stochastic differential equations that take into account a deterministic RF electric force and the random interaction with the neutral atom background. In addition, wall and ionizing collisions are modelled as discrete events.

The tools allow performing batches of simulations with different wall coating materials and gases, and have produced results in good agreement with experimental and theoretical data. The different output forms generated at run-time have proven to be very useful in order to analyse the different discharge processes. The tools are valuable for the selection of the most promising coating materials for the construction of the waveguide, as well as for the identification of safe operating parameters.

1 Introduction

The Multipactor (MP) [4, 26] and Corona (CR) [18] effects are electric discharges produced in radio frequency (RF) devices (typically waveguides) which may cause their inutilization.

*Work sponsored by the ESA, TRP activity program 17025/03/NL/EC: Surface Treatment and Coating.

In aerospace components, the electric discharges are caused by an initially small number of electric charges (mainly electrons) associated with cosmic rays or natural radioactivity, which are accelerated by the RF field and collide either with the waveguide walls (ripping new electrons from the material) or with the neutral atoms of the gas inside the device producing ionization. Both processes may multiply the free electron population until an electron avalanche develops, which may damage the waveguide [2, 18].

In MP, the discharge occurs at vacuum, and is caused by the collision of electrons with the walls. In CR, the discharge occurs at low pressures, with the presence of a gas in the waveguide and is produced by ionization of the gas neutral atoms. For certain pressure ranges, we may find both kind of processes (ionization and wall collisions) contributing to the discharge. This region is known as Multipactor Plasma [11].

In order to prevent from such discharges in the working operations of satellite devices, extensive laboratory testing has to be performed with different gases, material waveguide coatings, pressure ranges and RF frequency conditions. The objective of such testing is to select the best coating materials able to suppress the discharge, and to predict the safe operating voltages and frequencies. These experiments are time consuming and costly, taking into consideration that the location of the breakdown discharge voltage usually results in the inutilization of the testing sample. Therefore, recently, considerable effort is being spent in formulating physical models and building tools able to perform computer simulations of these phenomena [1, 8, 15]. Ideally, such tools should be useful from the engineering point of view, for the support of decision making in the device design, as well as from the scientific point of view, to understand and analyse the different processes involved in the discharge.

We have developed two simulators: MEST [15] (Multipactor Electron Simulation Tool) and CEST (Corona Electron Simulation Tool) with the objective of studying the discharge conditions, and to help in the selection of good coating materials for the inner walls of the waveguide to avoid the appearance of these discharges. Both simulators implement two novel physical models, with the main characteristic that the electrons are individually modelled and tracked. In the case of MEST for studying the MP effect, we follow a discrete-event simulation, where the events are the collisions of each electron with the walls, and taking advantage of the fact that the electron trajectory can be analytically computed, as we use a parallel plates geometry. In the case of CEST for CR, we use a hybrid simulation, where each electron trajectory is modelled using the Langevin differential stochastic equations [7]. The equations incorporate a deterministic RF field force and a random component to model the interaction with the gas. In addition, two contingent events may occur: collision with the walls and ionization of a gas atom.

This microscopic, individual-oriented simulation (where each electron is separately modelled) contrasts with most simulation approaches, where a macroscopic model of the phenomena is used [17, 22, 28], or simplifications are performed with generalized particles, made of an aggregation of particles (like in Particle-in Cell –PIC– simulators [1]). The use of a microscopic model offers several benefits, such as the possibility of obtaining richer output data from the simulation, for example, the number of collisions of each electron, MP modes [9] for each electron, etc. Note however that several simplifications had to be made in our models to keep them computationally tractable, so that they are only valid to study the phenomenon up to the discharge point, and the Corona model is only valid in certain frequency and pres-

sure ranges. They are only intended to predict the thresholds for the RF discharges. Their essential drawback is that, contray to PIC simulations, the space charge effects are neglected and therefore are valid as far as the number of charged particles remains small and the RF electric field dominates, see section 3.2 for further details.

In both tools, MEST and CEST, we have achieved results that show good agreement with theoretical and experimental data. We have also performed cross-validation of the simulators, and remarkably, at very low pressures, CEST and MEST provide very similar results (even if the underlying models are very different). Both tools provide run-time information about different simulation values, which are very helpful in understanding the dynamics of the discharge. This is especially useful in CEST, where at some pressures both, ionization and wall collisions are present in the discharge. In this way, the simulators reduce the need of performing real experiments, much more costly in resources and time.

Paper organization. Section 2 describes the MP and CR effects. Section 3 presents the models for both tools, while Section 4 shows the simulation techniques we have used. Section 5 introduces the main features of the tools. Section 6 presents the results obtained with the simulators, and compares with experimental an theoretical data. Section 7 compares with related research, and finally Section 8 ends with the conclusions and future work. The emphasis of this paper is more on CEST, and in its comparison with MEST, as some results about MEST have already been published [15]. We include however a description of MEST in order to make the paper self-contained, and because the wall-collision model proposed for MEST has been reused in CEST.

2 Multipactor and Corona Discharges

Multipactor. In the MP effect [4, 9, 26], the discharge is produced in vacuum, and thus the production of new electrons is caused by the collisions at the walls of a small initial population of electrons. These are accelerated by the RF field present in the waveguide. When the collisions at the wall synchronize with the field [9], an electron avalanche (MP) is produced.

Thus, a critical factor for studying MP is the understanding of the electron-wall collision process. Different coating materials present dissimilar properties regarding the production or absorption of electrons. In this respect, materials are characterized by the secondary emission yield (SEY), which gives the average number of produced electrons in each collision. When an electron impacts a wall, it can be absorbed, elastically or inelastically reflected (backscattered), or it can generate a number of true secondary electrons. In the case of backscattering collisions, both produce one single electron. In elastic collisions, the incoming electron is perfectly reflected with no energy loss. In the case of inelastic collisions, the electron penetrates into the material, scatters from atoms inside the material, and is reflected out with energy loss. These electrons are sometimes called re-diffused [6]. In the true secondary emission case, the electrons interact with the material in a more complicated way, and more than one electron may be produced.

The MP effect is studied for different coatings through $V - f \times d$ maps showing the discharge region. Figures 6 (left) and 12 show examples of these maps. The inner part of the curve is the region where MP discharge develops, while the outer part is the safe operating

area.

Corona. The CR effect is a local electric discharge initiated by gas ionization. This electric breakdown is produced with gas pressures lower than ground levels, caused by the progressive outgassing of the entire RF system with the increasing altitude reached by the spacecraft. According to the outgassing process of spacecraft systems with altitude, the CR effect typically develops between 60 and 80 Km, when the Telemetry, Tracking and Command subsystem inside communications satellites is switched on [3]. This electric discharge takes place under sharply non-uniform electric fields and is initiated again by a very small number of electric charges (mainly electrons) [18]. These seeding charges are accelerated by the RF electric field, and their subsequent collisions with neutral atoms resulting in ionizations produce the multiplication of charges in the gap between the conducting walls. The involved neutral gas pressures in CR discharge are several orders of magnitude higher than in MP or high vacuum electric discharges. In consequence, the mean free paths for ionizing and elastic collisions are shorter than the typical waveguides gap sizes.

At high enough pressures, electrons cannot reach the walls due to the high distortion in their trajectories caused by the collisions with neutral gas atoms. Thus, ionization is the only process of the discharge. However, for lower pressure ranges, electrons can be produced both at the walls and by ionization. As stated before, at even lower pressures, electrons are only produced at the walls. Thus, in studying CR, one has to characterize both the coating materials of the walls and the relevant properties of the gas inside the waveguide for the ionization process.

The CR effect is studied for different coatings and gases through the so called Paschen curves [18], which are $V - p$ discharge maps. Some examples can be found in Figures 9, 16 and 18. The lower part of the curve are safe operating zones where no discharge occurs (however at low pressures, there is a safe zone at high voltages, see Figure 9). One of the interests of these maps is the investigation of the minimum combination of voltage and pressure which produces a discharge.

3 The Models

In both models we have made a number of simplifications, suppressing physical processes which were not deemed relevant for the discharges. In this way, we consider a parallel plates geometry for the waveguide, with infinite or finite dimensions in the xy axis. One plate is located at $z = 0$ and the other at $z = d$, thus d is the plate distance. We consider a uniform sinusoidal RF field perpendicular to the plates, given by:

$$E_z(t) = E_0 sin(\omega t),\ E_x = E_y = 0 \tag{1}$$

$$E_0 = -V_0/d,\ \omega = 2\pi f \tag{2}$$

We do not consider the internal electric field generated by the newly produced electrons and gas ions, as it is negligible with respect to the external field. In addition, we are only interested in simulating up to the beginning of the discharge. Moreover, in the case of CR, the neutral gas atoms screen these inter-electron effects. This means that the only influence

for the electron trajectory is the RF field and, in the case of CR, the neutral gas background. Border effects due to the geometry in the RF field are not considered. For the case of finite parallel plates, when an electron leaves the geometry, it is eliminated from the simulation.

3.1 The Multipactor Model

In this section, we give an overview of the MP model, for further details the reader is referred to [15]. The main aspect of the MP model is the collision of an electron with the wall. A collision can generate zero (absorption) or more electrons. The average number of electrons produced in a collision (the SEY) is typically modelled as a function depending of the energy of the primary electron (E_p). Figure 1 shows a typical SEY curve, where E_1 and E_2 are the energy values in which the SEY is equal to 1. E_{max} is the energy in which the SEY reaches its maximum value (σ_{max}). These parameters are typical in the literature [26] for characterizing the SEY of a material.

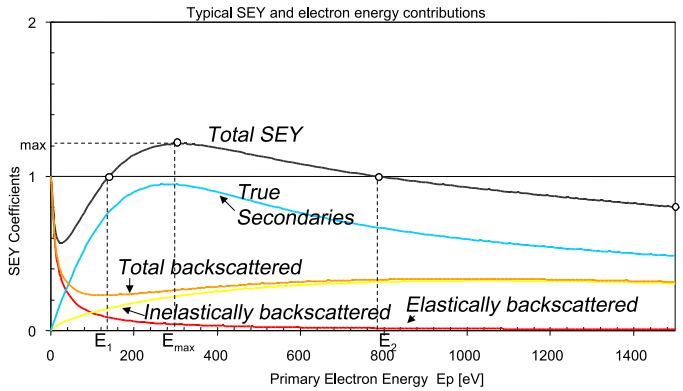

Figure 1: Typical SEY.

We have proposed a more elaborate SEY model [15] in the line of [6], where, in addition to the primary electron energy (E_p), we take into account its angle (ϕ) and the contributions of each kind of collision: true secondaries, elastically reflected and inelastically backscattered. Materials are characterized by 14 parameters, including for example its atomic number, or the surface cleanliness (see [15] for details, and the right of Fig. 5). First, we model each contribution with a dependency on the primary electron energy, and then add the angle dependency to obtain $\eta(E_p, \phi)$ (inelastically backscattered), $\varepsilon(E_p, \phi)$ (elastically backscattered) and $\delta(E_p, \phi)$ (true secondaries, see [15] for details). These expressions allow calculating the collision probabilities. Thus for inelastic collisions, it is $P_b(E_p, \phi) = \eta(E_p, \phi)$, for elastic collisions is $P_e(E_p, \phi) = \varepsilon(E_p, \phi)$, and for the case of true secondary collisions is $P_s(E_p, \phi) = 1 - P_e(E_p, \phi) - P_b(E_p, \phi)$.

After calculating the collision type, we have to calculate the number of output electrons and their energy. In the case of backscattering collisions, both produce one single electron. In elastic collisions, the incoming electron is perfectly reflected with no energy loss. For the inelastic ones, we calculate the electron energy as an inverse cumulative probability function [15] that ensures energy conservation.

In the true secondary emission case, a random number n of electrons are produced. This number is modelled as a probability $P_n(E_p, \phi)$ with Poisson distribution $Poisson_n(\lambda) = e^{-\lambda}\,\lambda^n/n!$, where λ is the distribution average, given by:

$$\lambda(E_p, \phi) = \frac{\delta(E_p, \phi)}{1 - \varepsilon(E_p, \phi) - \eta(E_p, \phi)} \tag{3}$$

Once the number of output electrons has been fixed, its energy is sequentially calculated by another inverse cumulative probability function, ensuring that the total energy is equal or less the incoming electron energy (E_p).

The procedure calculates the output electron angles as follows. We consider emission angles θ with respect to the inward normal to the xy plane, and ζ in the xy plane. In the case of a backscattering collision, the output angles are $\theta = \phi$ (where θ is the output angle) and $\zeta_{out} = \zeta_{in}$. In the case of a true secondary electron, the angles are calculated using the *cosine law* distribution: $\theta = arcsin(\sqrt[2]{x^2 + y^2})$, $\zeta = arctan(y/x)$, where x and y are random numbers with uniform probability in $[-1, 1]$, such that $x^2 + y^2 \leq 1$.

3.2 The Corona Model

In the CR model, electrons are again under the influence of the RF electric field, but they are also randomly scattered by elastic collisions with the atoms of the neutral gas. It is not computationally feasible to explicitly represent each atom in the gas, therefore, our approach is to include this influence in the equations that govern the electron trajectory. We have taken into account two forces to model the interaction of the electron with the gas: a friction force F_r, representing the resistance to electron advance and a random force F_d, representing the scattering of the electron.

The friction force is given by $F_r = -m_e \nu_m u_e$, where m_e is the electron mass, u_e is the electron velocity and ν_m is a friction coefficient given by $\nu_m = n_a \sigma_m u_{rms}$. In this latter expression, n_a is the neutral atom density, σ_m is the averaged cross section for momentum transfer and $u_{rms} = \sqrt{2eV_{RMS}/m_e}$ is the electron speed in RMS (Root Mean Squared), where for a sinusoidal voltage, $V_{RMS} = V_0/\sqrt{2}$.

The random force is given by $F_d = C \cdot \Gamma(t)$, where C is a matrix that accounts for the change in direction of the electron speed originated by the collisions with neutrals, and the elements of vector $\Gamma(t)$ are gaussian random variables. As successive collisions are statistically uncorrelated, these variables satisfy:

$$< \Gamma_i(t) >= 0 \tag{4}$$

$$< \Gamma_i(t)\Gamma_j(t') >= \delta_{ij}\delta(t - t') \tag{5}$$

where $< \cdots >$ is the ensemble average [7], and $i, j = \{x, y, x\}$ are the spatial coordinates. Matrix C is diagonal (with diagonal elements having equal value) due to the uniform spatial distribution of the gas atoms, and because the electron scattering is isotropic. The value of its diagonal elements is given by $C_{ii} = \sqrt{2K_B T_e/m_e}\sqrt{\nu_m}$, and the expression $K_B T_e$ is calculated from the average kinetic energy of the electrons at each time step.

Altogether, each electron trajectory is given by the following Langevin equations [7] of motion:

$$\frac{dr_e}{dt} = u_e \tag{6}$$

$$\frac{du_e}{dt} = -\frac{e}{m_e}E(t) - \nu_m u_e + C \cdot \Gamma(t) \tag{7}$$

In addition, the model considers two kinds of collisions for the electrons: wall and ionization collisions. In the first case, the collisions are treated as in the MP model of previous subsection. For an ionization to be produced, the electron has to traverse a path larger than the collisional mean free path for ionizations (λ_I), and its energy should exceed the ionization threshold E_I (a gas dependent constant). We take the mean free path to be constant and gas dependent. It is given by $\lambda_I = 1/(\sigma_I n_a)$, where σ_I is an approximation of the ionization cross-section $\sigma_I(E_p)$ of the gas.

The result of the ionization collision is a newly generated electron at rest, located at the same point where the ionizing electron was placed. The energy of the latter diminishes by an ionization energy E_I, thus preserving the overall energy, while the newly generated electron moves under the influence of the RF electric field. The influence in our model due to the generated ions is neglected, as in the works of [20, 21, 24, 25].

The presence of runaway electrons has been ignored in CEST because the direction of the electric field oscillates with typical frequencies of the same order of magnitude as the involved electron collision frequencies. In addition, the effective cross section for electrons also involves the excitation and ionization cross sections and decreases with the electron speed slower than the critical threshold for the runaway effect in the cross section for elastic collisions [19, 23, 30].

Model Limitations. The practical limits for CEST depend on the collisional cross sections of the neutral gas, the waveguide gap d, the RF peak amplitude V_o and wave frequency f. The time and length scales for CEST are characterized by two dimensionless ratios, the quotient d/λ_{ea} between d and the electron elastic mean free path λ_{ea} as characteristic length and the ratio ν_{ea}/f between the elastic collision frequency and the RF signal frequency for the time scale. Both are depicted in Figs. 2 and 3 as a function of the pressure of Argon for actual values of d employed in the experiments and the RF frecuencies of interest between 1.5 and 31.0 GHz.

The collision frequency ν_{ea} increases with the neutral gas pressure and for $\nu_{ea} > f$ the electrons collide faster that the RF electric field reversal. This leads to an upper bound for time scale that restricts the CEST simulations in Fig. 2 below the horizontal dotted line where $f \geq \nu_{ea}$. For the higher frequency available of 31 GHz, the maximum pressure is 1 mB and the corresponding RF amplitude of $V_o = 10^2$ volts. This gas pressure also limits in Fig. 3 the possible values for the gap size to $d \simeq 10 \times \lambda_{ea}$. Our tool detects the limits when $\nu_{ea} = f_{RF}$, $d = 10 \times \lambda_{ea}$ and $d = 100 \times \lambda_{ea}$ and warns the user about possible false results, as shown for example in Fig. 9.

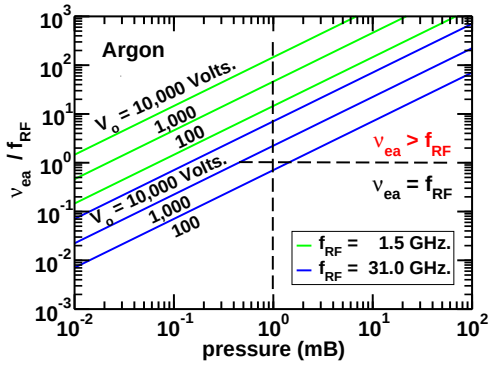

Figure 2: The ratio ν_{ea}/f as a function of the Argon pressure for the RF frequeny range between $1.5 - 31.0$ GHz. The dotted horizontal line indicates when the electron collision frequency $\nu_{ea} > f$ and the vertical dotted line corresponds to the maximum pressure for this particular CEST simulation.

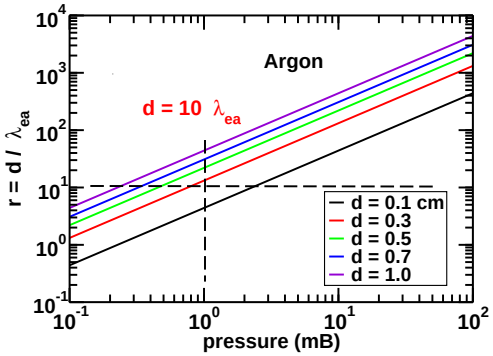

Figure 3: The ratio d/λ_{ea} as a function of the Argon pressure where λ_{ea} is the mean free path for elastic collisions. The dotted horizontal line indicates the gap distance $d \sim 10 \times \lambda_{ea}$.

4 The Simulation Procedure

In the design of both simulators we have followed the object-oriented paradigm, where each electron is represented as an object. For the simulation of the MP model, we have used a typical discrete-event simulation scheme [5], summarized to the left of Figure 4. The simulator uses a queue for the time ordering of the events. These events have associated the entity (electrons in this case) which produced them. The main simulation loop consists on taking the first event, advancing the simulation time and executing the event specification (over the associated electron), which may produce the scheduling of new events in the future.

In our case, the relevant events (those which increase the simulation time) are the collisions of the electrons with the walls. We can use this kind of simulation because the next collision time of each electron can be calculated analytically. When processing each event in the queue, the simulator accesses the electron causing the collision, and calculates the parameters of the resulting electrons from the collision. If some are generated, the time of their collision is calculated and the collisions are inserted in the event queue. If the surface absorbs the

electron in the collision, the electron is eliminated from the simulation.

At the beginning of the simulation, a population of electrons is generated with a normally distributed energy. All start at one of the plates and are assumed to have impacted that plate at a random time in the first RF field period. In this way, this collision initial time is used to initialize the event queue.

As it can be noted, we do not move all the particles simultaneously (as in the PIC codes [1]), but each electron is moved independently to its next collision. The electron state does not need to be calculated or saved in intermediate instants, but only at the collisions. Note also that having two or more simultaneous events is possible, and they are stored in the order in which they are produced. In fact, they can be processed in any order, for, in our case, the events already in the queue do not depend on one another.

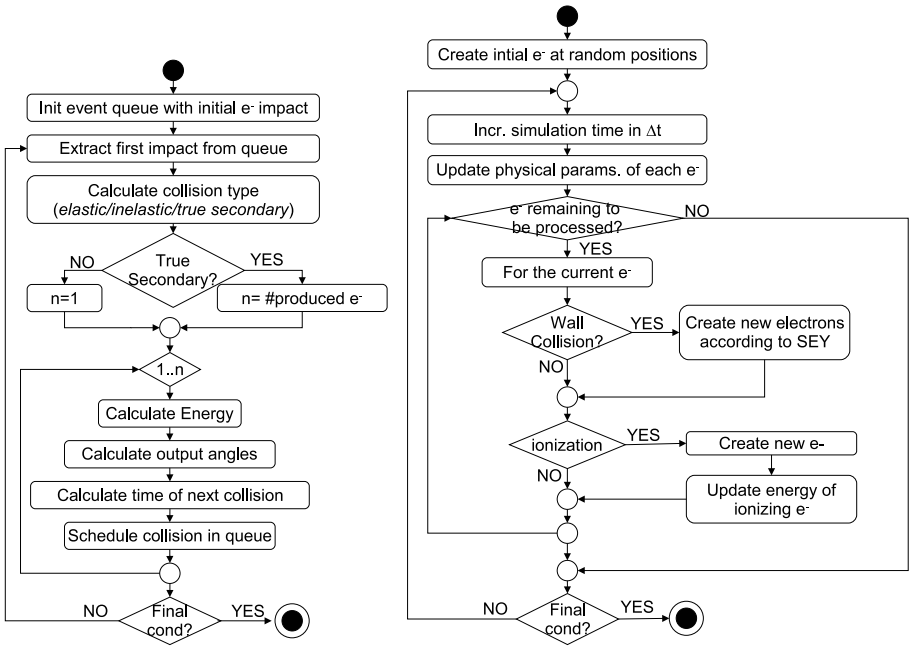

Figure 4: MP Simulation Procedure (left). CR Simulation Procedure (right).

The simulation of the CR model is continuous, where the stochastic differential equations given in 6 and 7 have to be integrated for each electron, and where contingent events may occur. For the solution of the stochastic equations, they are made dimensionless using the plate distance d for the length scale and $\tau = 1/T$ for the time scale (where T is the RF period), and integrated using the Milstein stochastic integration scheme [10]. As events are contingent (i.e. they cannot be programmed in the future), there is no need for an event queue.

The right of Figure 4 shows the CR simulation scheme. Initially, a number of seeding electrons are randomly distributed in an electrode. To guarantee the random initialization, they start with energy from a Maxwell Boltzmann distribution, at a random position in the gap (z-coordinate of the waveguide). Then, for each electron, at each time step, in addition to update their physical parameters (by performing the Milstein integration), we check whether

some of the two possible events hold: collision with the walls and ionization. In the first case, the collision is treated as in the MP simulation (i.e. absorption can occur, or new electrons can be produced, and then introduced in the simulation). The second event type was described in previous section, and generates a new electron at rest.

Note that as this simulation is driven by the integration of the differential equations, it is usually less efficient than the previous discrete-event one, because the simulation time is incremented at fixed steps of Δt in the CR simulation.

5 The Tools

In this section we present the main features of the tools, and stress their usefulness for the investigation of the different processes in the discharge. Both simulators have been implemented in C++, using the MFC framework.

5.1 MEST

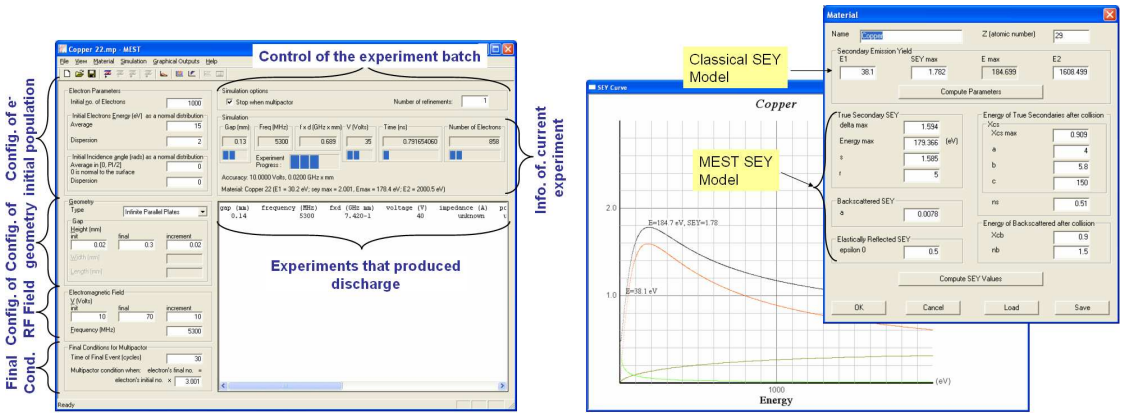

Figure 5: MEST Main Window (left). Coating Material SEY Configuration (right).

The left of Figure 5 shows the MEST main window. The left part of the window allows entering the initial conditions of the simulation (initial number of electrons, average energy and dispersion of the initial electrons and their initial angle, see the inscriptions in the figure). It is possible to specify intervals for the gap distance d, and gap voltage V, such that one simulation is performed for each combination of their values. The lower box ("Final Conditions") permits specifying a final time for the simulation as well as final conditions based on the number of electrons remaining with respect to the initial population. This condition is needed in order to distinguish experiments that resulted in discharge or electron absorption.

Box "Simulation options" to the right allows choosing simulating all combinations of V, f and d, or looking for the lower and higher values of these parameters which produce discharge. In the latter case, only the borders of the discharge $V - f \times d$ region are calculated but not the inner points, and the user can select the degree of accuracy of such borders. The text boxes inside the panel "Simulation" show the simulation results as they are computed,

while the text box at the bottom prints one line with the results for each simulation that produces discharge. The line shows information about the conditions of the experiment (gap, frequency, voltage, power, initial number of electrons), and the simulation results (phase of first collision, multipactor, final simulation time, final number of electrons, impedance and susceptibility).

The properties of the material are entered using a separate dialog box, as shown to the right of Figure 5. We can use two sets of parameters: the classical one based on E_1, E_2 and σ_{max}; or the more complete we proposed in [15] with 14 parameters. MEST is able to approximate one parameter set given the other one. The SEY curve for the material can also be visualized, showing the three main contributions, as the right of Figure 5 shows.

Once the experiment and the properties of the material have been set, the simulation can start. The main output window provided by MEST is the $V - f \times d$ discharge region. The left of Figure 6 shows a discharge region for Copper. In this map, we use different colors to indicate the probability of discharge. We calculate a qualitative measure (which we call *susceptibility*), taking into account the rate of change of the number of electrons (positive if they increase) with respect to time. In this way, when a discharge occurs, the quantity is positive (the bigger, the more probable the discharge is) otherwise it is negative (the bigger in absolute value, the more probable the absorption is). In the graphic, we use orange, orange-red and red for increasingly probable discharge, and green, blue-green, blue and dark blue for decreasingly probable discharge. Thus, dark-blue corresponds to a negligible probability of discharge, while red depicts a strong probability of discharge.

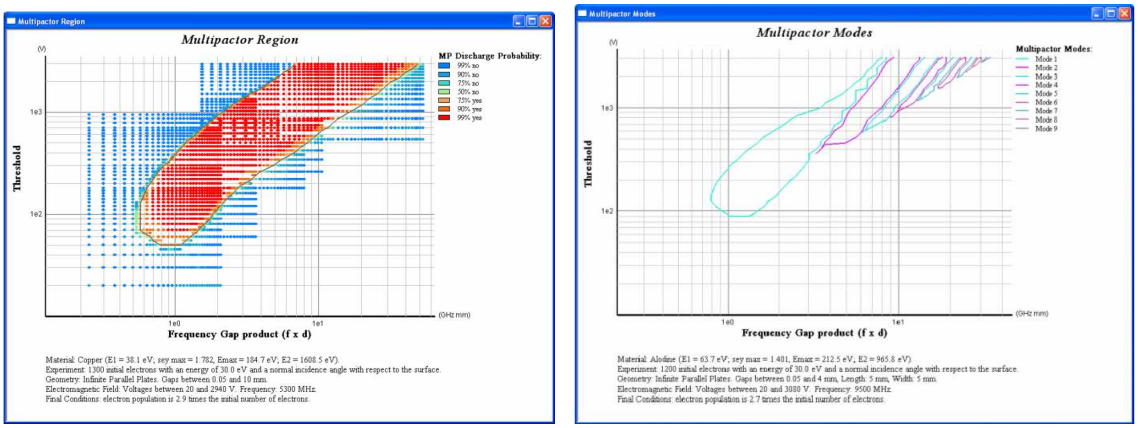

Figure 6: Discharge Region for Copper (left). MP Modes for Alodine (right).

MEST can calculate the MP modes for the discharge region if the inner points of the region are simulated. The modes are defined according to the Hatch and Williams theory [9] as the integer number of RF periods an electron takes to go from one impact to the next one, plus one. Thus, mode 1 is just a semi-period, as it is the minimum time an electron takes to go from one side to the other of the geometry. The right of Figure 6 shows the modes for a simulation with Alodine, in which the first nine modes are shown.

MEST allows observing the evolution of the number of electron at run-time, for each experiment. The windows in Figure 7 show two different experiments for Alodine and Alu-

minium. The one to the left starts with 2000 electrons, while the one to the right with 1000. In both cases, there is a transitory period at the beginning of the simulations, where the number of electrons changes erratically. This is due to the fact that some initial electrons are not synchronized with the frequency of the RF field, as they are uniformly distributed in the first period of the RF field. In the left window, the number of electrons increases in steps of 3 RF periods approximately, due to the fact that under the experiment conditions, resonant electrons take about three periods to reach the opposite plate. As stated before, the number of semi-periods taken by an electron to go from one plate to the other is related to the MP mode. The simulation shown in this window resulted in discharge.

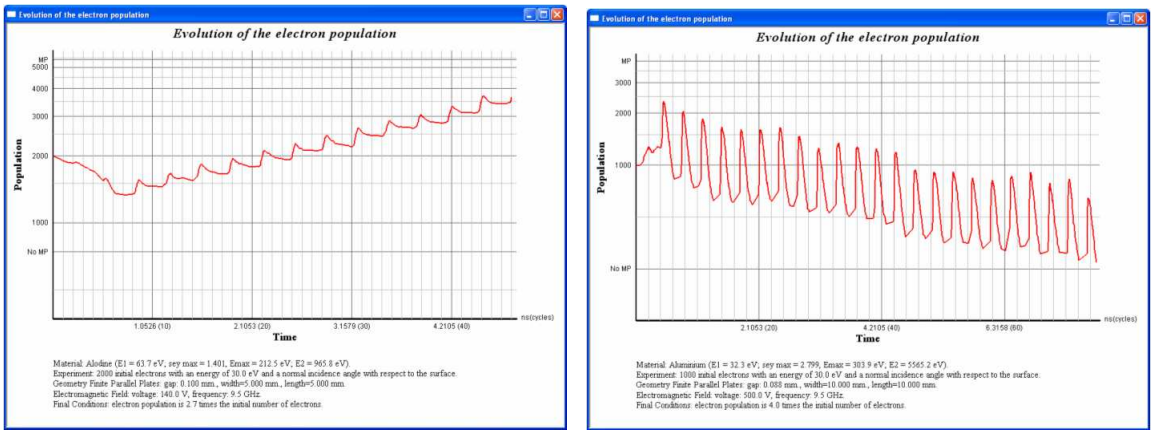

Figure 7: Evolution of Number of Electrons for a Simulation of Alodine, which resulted in Discharge (left). Evolution of Number of Electrons for a Simulation of Aluminium, which resulted in Absorption (right).

For the window to the right, the final condition for discharge was set to be 4 times the initial population. Note that in this case, even though the number of electrons initially increased, absorption occurred at the end. If a smaller final condition for discharge had been placed, the simulator would have incorrectly signaled a discharge (due to the initial transitory effect). Thus, as the maximum increment of electrons in each RF peak depends on the maximum SEY (σ_{max}) of the coating material (Aluminium in this case, with $\sigma_{max} = 2.799$), a final condition bigger than this value has to be chosen.

MEST also allows observing an animation of the electron cloud. This feature is also present in CEST (see the right window in Figure 11), and will be explained in next subsection.

5.2 CEST

CEST follows a similar approach to MEST and its main window is shown in Figure 8. As in MEST, the left part of the window is used to enter the initial conditions of the simulation (initial number of electrons and initial electronic temperature). The user can also select between two types of experiments: discharge zones, and discharge curve. In the first case, a $V - p$ curve (called Paschen curve) is generated, where the voltage and the pressure are the free variables (and the gap is fixed), for which an interval should be specified. In the second case, the free variables are the voltage and the gap (and the pressure is fixed), and a $V - f \times d$

plot similar to the ones obtained for MEST is generated. In both cases, one simulation is performed for each combination of values of the free variables.

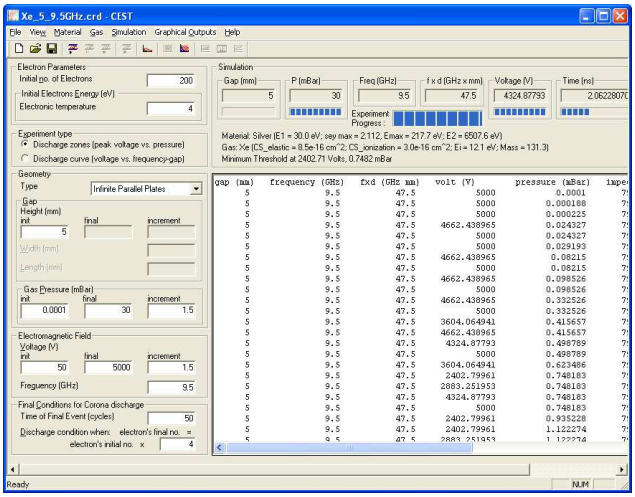

Figure 8: CEST Main Window.

As in MEST, the box labelled as "Simulation" on the top right shows data corresponding to the current simulation, and concerning the progress of the total batch of experiments. It also shows the current material and gas properties, as well as the experiment (in the case of a discharge zone experiment) which produced a discharge with lower pressure at the current moment. Below the previous box, CEST shows the data corresponding to experiments that resulted in discharge. The same data as in MEST is included, and in addition the pressure.

In a similar way as in MEST, the coating material properties have to be specified. In addition, the gas has to be characterized by providing its molecular mass, its total elastic and ionization cross sections and the first ionization energy. Together with the simulation results, CEST is able to calculate a semi-empirical Paschen curve (taken from [18]). This is an expression, empirically fitted, which depends on two values A and B, which model the dependency on the coating material and the gas. If no such data is known for a certain gas, then its semi-empirical Paschen curve is not plotted.

Once the initial and final conditions, as well as the gas and the material properties have been introduced, the experiments can be executed. As stated before, CEST performs an experiment for each combination of voltage and gap (with fixed pressure and frequency) in the discharge curve mode. In the discharge zones mode, the code executes one simulation for each combination of pressure and voltage (with fixed gap and frequency).

Once the first simulation has finished it is possible to graphically visualize the experiment results in the $V - P$ (the Paschen curve) or $V - F \times d$ maps. As new experiments finish, results are dynamically added to the map. Figure 9 shows an example of Paschen curve. As in MEST, each point corresponds to an experiment, its color depicting the occurrence or not of discharge and its strength. In addition to the points corresponding to experiments, the semi-empirical curve proposed by [18], and the valid simulation ranges are plotted. These ranges correspond to the limits explained in section 3.2: $\nu_{ea} = f_{RF}$ $(soft)$, $d = 10 \times \lambda_{ea}$ $(medium)$ and $d = 100 \times \lambda_{ea}$ $(hard)$.

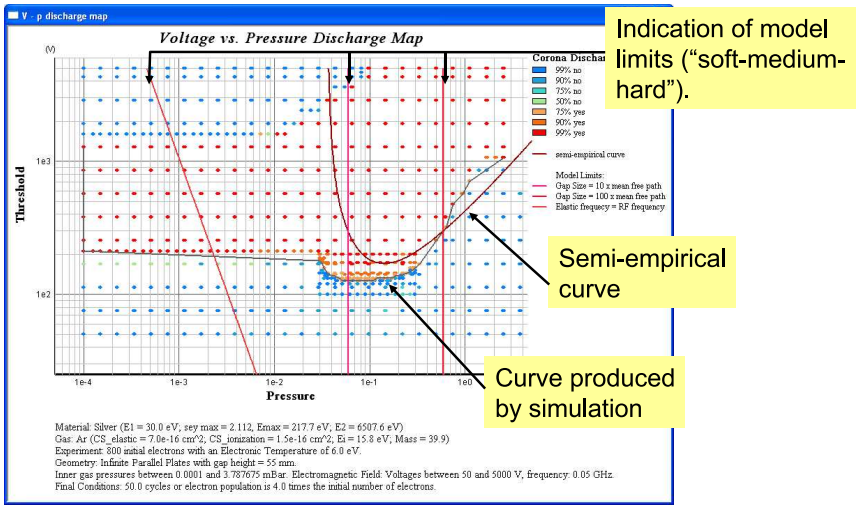

Figure 9: $V - P$ Paschen Discharge Curve Produced by CEST for Argon and Silver coating.

During the simulations, it is possible to check the evolution of the electron population, as Figure 10 shows. The black line shows the total number of electrons. The red line depicts the initial electrons. The green line shows the electrons produced due to collisions at the walls. The blue line shows the electrons produced due to ionization of neutrals. In the case of the left window in the figure, all remaining electrons have been produced due to collisions at the walls. This is due to the fact that the pressure in the experiment is low. As in MEST, for very low pressures it is possible to observe the resonance peaks of increasing electrons, which is related to the MP mode. Even when in CEST the simulation model is totally different, the results of MEST are recovered. The window to the center of the figure shows an experiment at higher pressures, where electrons are produced both at the walls and due to ionization. Here the oscillations due to the RF field are less visible. Finally, the window to the right shows an experiment where all electrons are produced by ionization (at higher pressures). Note that at this pressure range, discharges occur extremely fast. This output window makes CEST an excellent tool for investigating the origin of the electrons producing the discharge.

It is also possible to obtain the run-time evolution of the average electronic temperature, which is related to the average electron energy. The left of Figure 11 shows a screenshot of this graphical output. This window can be used to investigate the correlation between discharge experiments and the evolution of the electrons energy. A periodic behaviour, caused by the sinusoidal RF signal, can also be observed.

As in MEST, CEST also allows observing the trajectories of the electrons during an experiment. However, in addition, we show in blue colour the electrons produced due to ionizations. The right of Figure 11 shows an experiment, which ended up in discharge, where most electrons are produced due to SEY. Electrons are plotted in different colours depending on the number of collisions they have experimented. This window is interesting to check the behaviour of electrons and their synchronization with the RF signal at low pressures. At higher pressures, electrons have less mobility, and we can observe growing clouds of new electrons emerging in small heaps due to ionization. Note however that the results

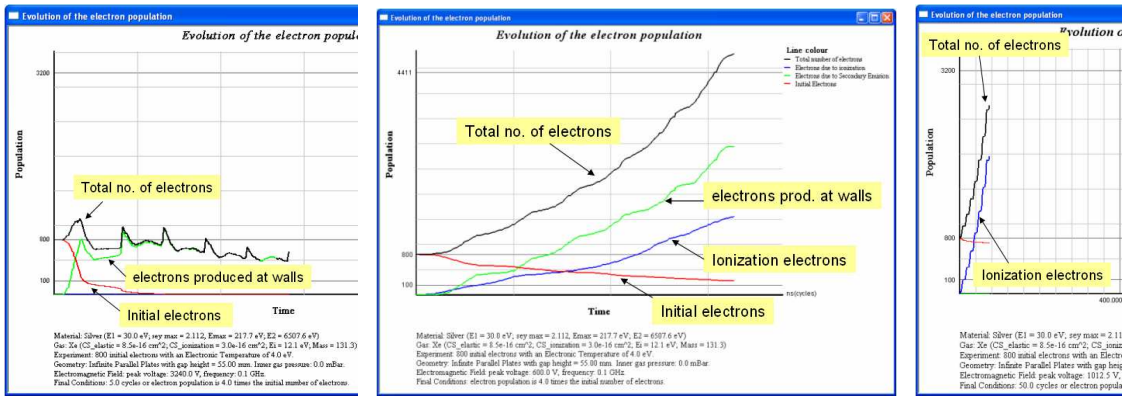

Figure 10: Evolution of the Number of Electrons. Low Pressures Zone (left). Intermediate Zone (center). Ionization Zone (right).

in this window have to be taken with some caution, because our model does not consider the interactions between electrons. This window should be used just as an illustration of the coupling between the RF signal and the electron cloud. Note however that as the simulation ends at the beginning of the discharge, the effect of electron interaction is negligible with respect to the external field.

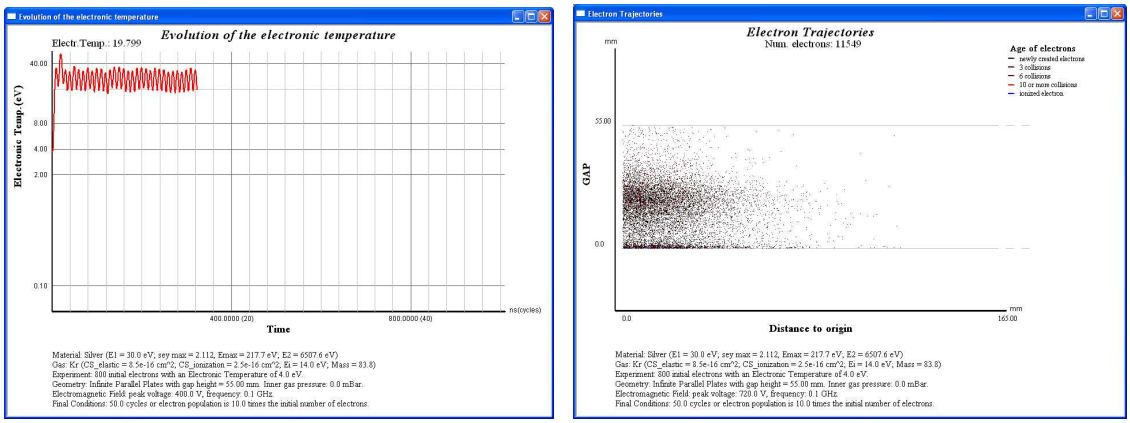

Figure 11: Evolution of Electronic Temperature (left). Evolution of Electron Cloud (right).

6 Results

Comparing MP Results with Theoretical and Experimental Data. We have tested the $V - f \times d$ discharge regions produced with MEST with both theoretically predicted regions (using the Hatch and Williams theory [9]) and experimental data (mainly from [29]). As an example, Figure 12 shows to the left the discharge region for Alodine predicted by the Hatch and Williams theory, where the red rectangles show experimental data from [29]. This graphic was produced with the Multipactor Calculator tool [16]. To the right, the figure shows the

discharge region produced with MEST, showing good agreement. However, we never were able to reproduce the lower-left peak predicted by the theory, but note that this has not been confirmed by experimental data. We believe that validating the degree of accuracy of this theory is a challenge for either experimental researchers or computer simulationists [14].

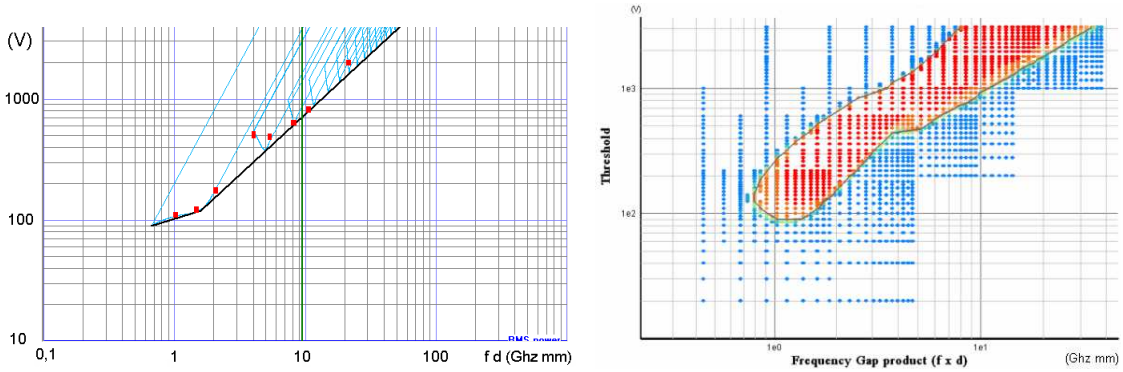

Figure 12:
Experimental data for Alodine from ESTEC, fitted with Hatch and Williams theory, produced with MP Calculator (left). $V - f \times d$ Discharge Region for Alodine with MEST

The MP modes obtained with MEST also show good agreement with the predicted modes of the Hatch and Williams theory, as shown to the right of Figure 6. The reader is referred to [15] for more exhaustive results of other coating materials.

Investigating the CR Discharge Processes at Different Pressures. CEST is useful to predict and understand the different discharge processes, mostly at the intermediate pressures region, where the discharge is caused by ionization and wall collisions. The next sequence of figures (from 13 to 15) show different $V - f \times d$ discharge regions for Argon and Stainless Steel coating at different pressures, with a frequency of 0.5 GHz. CEST allows studying the origin of the electrons causing the discharge. The left Figure 13 shows an experiment at low pressures, where all electrons are produced at the walls. This means that the inner gas is irrelevant for the discharge. The figure also shows the Paschen curve calculated by CEST, with a setting of $f \times d = 5$. The x coordinate with that value are shown at the background window, and it can be noted how the breakdown voltages agree at about $1000\,V$ (but the background voltages are peak-to-peak, that is why we obtain $2000\,V$).

The right of Figure 13 shows the change in the $V - f \times d$ discharge region once the pressure is increased to 0.025 mBar. At this pressure, the discharge region increases because electrons also start to be produced due to ionization. The left of Figure 14 shows the result of another pressure increase (to 0.1 mBar), which shows that in this region electrons are produced both at the walls and due to ionization. The Paschen curve shows that the experiments correspond to the intermediate region, where the curve starts to descend. Thus, the breakdown voltage for the indicated line of $f \times d = 5$ is slightly lower than in previous windows.

The right of Figure 14 shows an experiment with $P = 0.25$ mBar, in which all electrons are produced by ionization. In this way, the walls (and therefore their coatings and SEY properties) are no longer relevant for the discharge, being the type of gas the only factor. Note also, that this pressure corresponds with the bottom of the Paschen curve, thus for

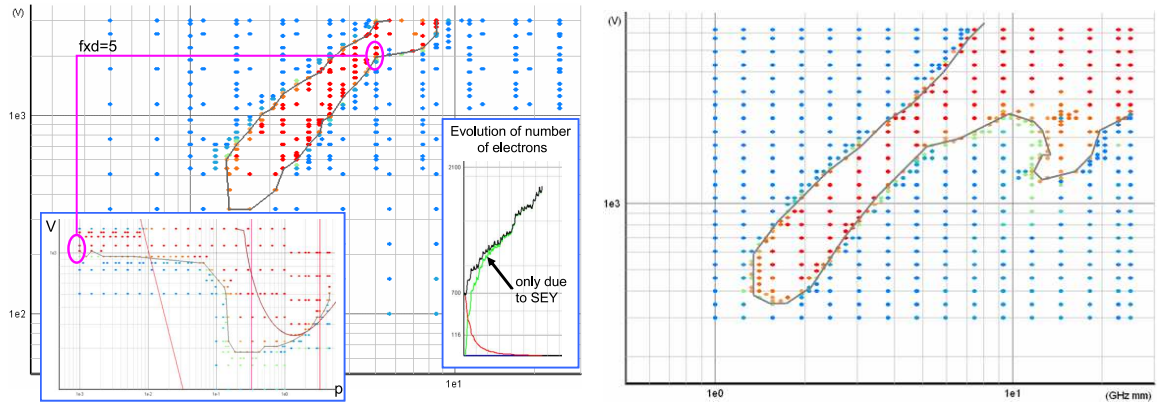

Figure 13:
Discharge Maps for Argon and Stainless Steel at Different Pressures. $V - f \times d$ Map at $P = 0.001$ mBar (left) and at $P = 0.025$ mBar (right).

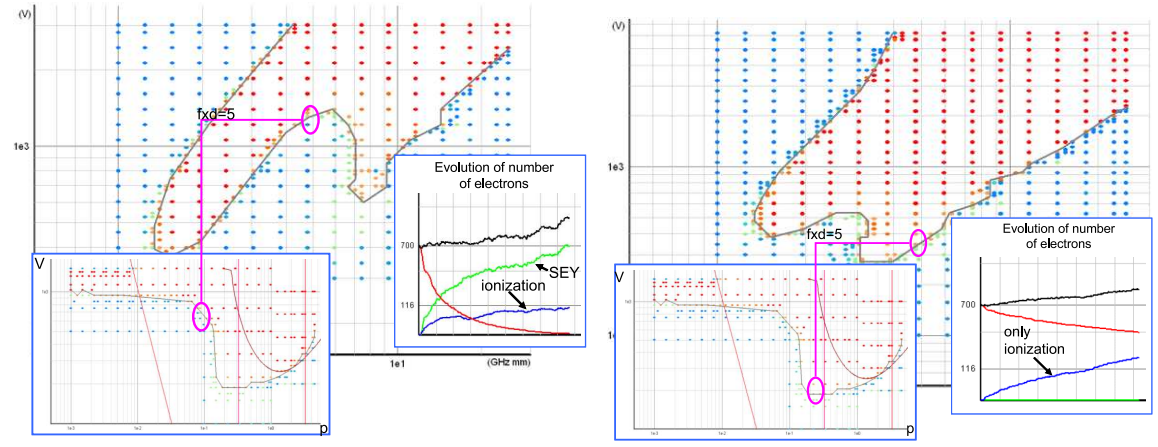

Figure 14:
Discharge Maps for Argon and Stainless Steel at Different Pressures. $V - f \times d$ Map at $P = 0.1$ mBar (left) and at $P = 0.25$ mBar (right).

$f \times d = 5$ we obtain even lower breakdown voltages than in previous windows.

The left of Figure 15 shows an experiment with $P = 1$ mBar, in which all electrons are produced by a ionization, as the evolution of the number of electrons shows. The experiment corresponds with the starting of the increase of the Paschen curve, thus showing slightly higher breakdown voltages than previous Figure 14 e.g. for line $f \times d = 5$. Finally, the right of Figure 15 shows another experiment with even higher pressures at 3 mBar. Note that overall, with increasing pressures up to 3 mBars, the safe operating area decreases: the breakdown discharge occurs for a larger range of voltages. Moreover, discharges occur for lower values of $f \times d$ and lower voltages. To the very best of our knowledge no other tool can perform this kind of experiments.

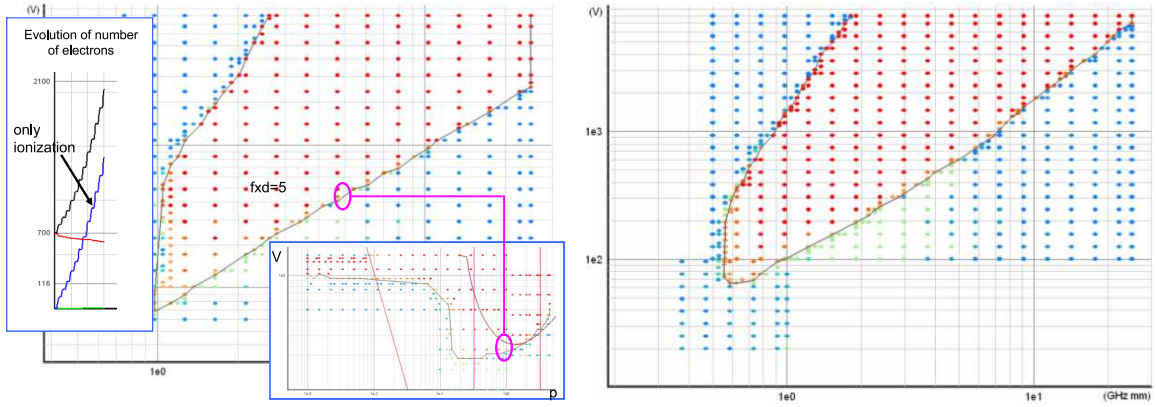

Figure 15:
$V - f \times d$ Discharge at $P = 1$ mBar (left) and at $P = 3$ mBar (right).

Comparing CR Results with Data from the Literature. We have also compared our results with experimental data obtained from the literature. For example, the left of Figure 16 shows a Paschen curve with the actual experimental data of [11] for parallel plates geometry with Stainless steel coating and Argon gas. The pressure is given in Pascals ($1\,Pa = 0.01\,mBar$). The right of the same figure contains the results of our simulations using CEST, which shows an overall good agreement. Note that the pressure in the right graphic of Figure 16 is in mBar. It is also remarkable the good agreement of the simulation results with the semi-empirical curve from [18].

Cross-Validating CEST and MEST. We have cross-validated CEST and MEST by performing $V - f \times d$ experiments at very low pressures with CEST and comparing the results with those obtained with MEST. The results are more than satisfactory as is deduced from the comparison in Figure 17. The window to the left shows an experiment with CEST using infinite parallel plates and silver coating at the walls. The RF frequency was 9.5 GHz at the neutral pressure of 10^{-4} mBar of molecular nitrogen. To the right, a graphic shows the results of the same experiment using MEST.

It is remarkable the excellent agreement between both results being aware of the fundamental differences between the models employed in both tools. This means that the CEST model is valid for MP at low pressures, when the collisional mean free path λ_{ea} becomes negligible and the ionization mean free path λ_I is so large that all electrons are produced

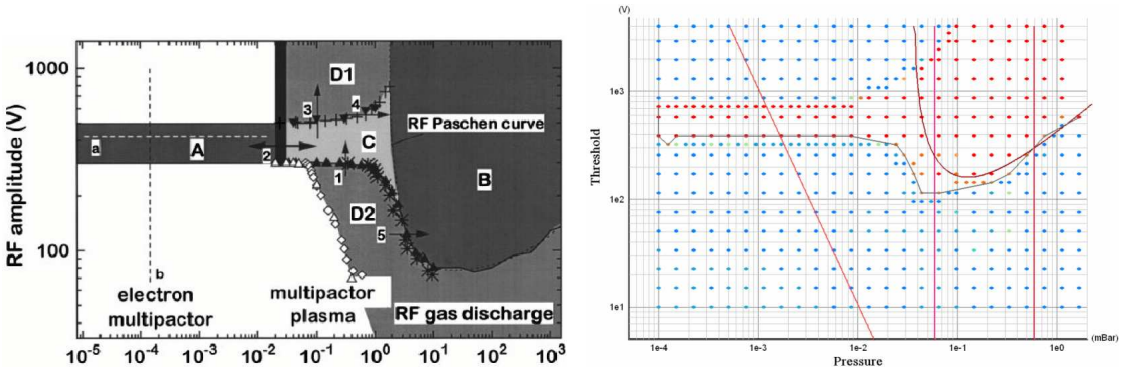

Figure 16:
Actual experimental data from [11]. Experiment with Ar, Stainless Steel, 50 MHz (pressure in Pa) (left). Same Experiments using CEST (pressure in mBar) (right)

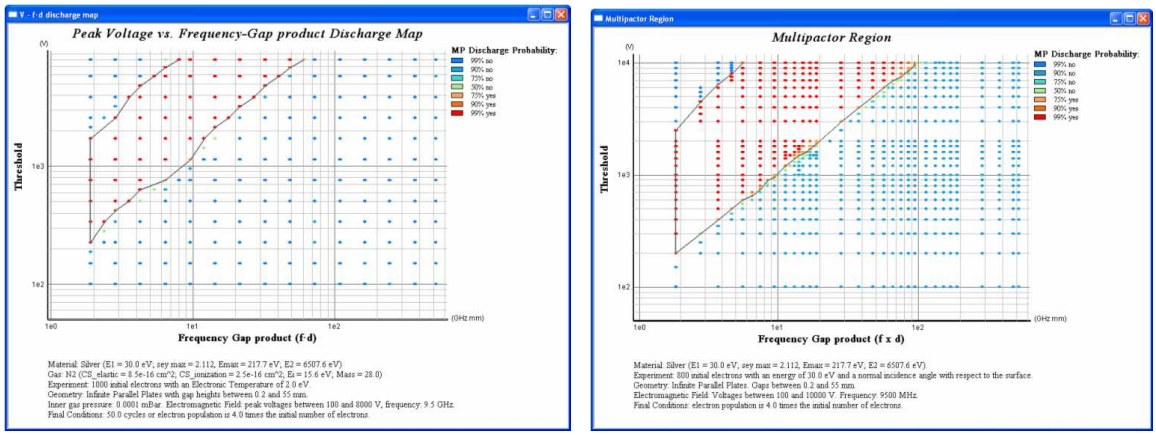

Figure 17:
Simulation with CEST: N_2, silver coating and f=9.5 GHz (left). Same Experiments using MEST (right)

at the walls. For very low pressures the electron motion becomes collisionless and therefore, the numerical calculations of the electron trajectory and speed become equal to the analytical calculation of these magnitudes used in MEST. In addition, because the models for the electron interaction with the walls are the same in both simulators, CEST reproduces for low very pressures the results obtained for multipactor with MEST simulator. Note however that for performing simulations in vacuum or very low pressures, it is better to use MEST, because it usually produces faster simulations (it is discrete-event based) and it produces information about the MP modes (see the right of Figure 6). On the contrary, CEST produces a run-time information with the evolution of the electronic temperature, not available in MEST.

CR Discharge Results for Different Gases and Coatings. CEST has been used to predict the discharge regions for several gases and coatings, at different frequencies. Although experimental data for comparison is missing (we could not find the data in the literature, to the very best of our efforts), it is remarkable the good agreement of the simulation results with the semi-empirical curve proposed in [18]. Figure 18 shows two results for Xe and N_2 at frequencies of 500 MHz and 9.5 GHz respectively with infinite parallel plates geometry.

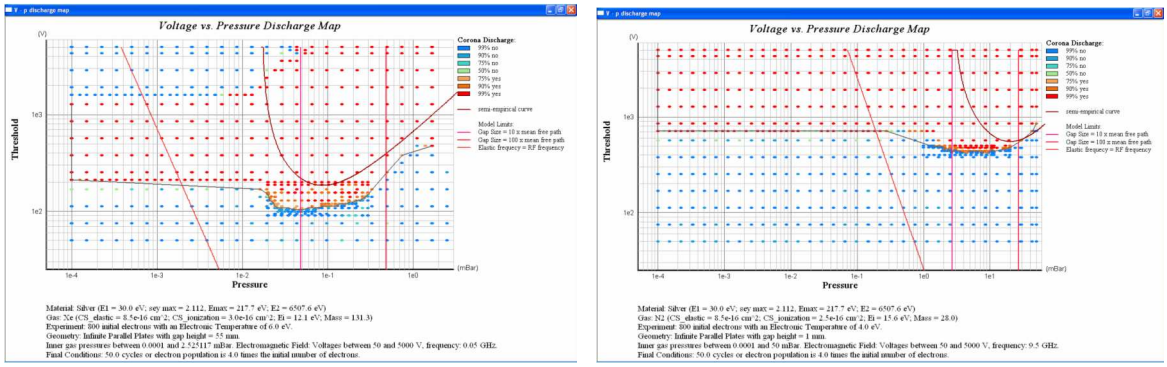

Figure 18:
Paschen Curve for Xe, Silver coating at the walls, gap=55 mm, f=50 MHz (left). Paschen Curve for N_2, Silver coating at the walls, gap=1 mm, f=9.5 GHz (right).

7 Related Work

There are many works that use the concept of "macroparticle" in the simulation. These codes are usually called Particle-in-Cell (PIC) [1]. Typical PIC simulations represent a large number of real particles by a vastly smaller number of macroparticles in order to make the numerical problem tractable. In plasma simulations, one macroparticle may actually correspond to 10^8 or 10^{10} physical electrons [27]. Some works following this approach are for example [12, 27, 17, 22] for the case of MP and [28] for the case of corona. See also [1] for a review of more sophisticated models including collisions with atoms.

In our case we do not need to use such macroparticles, as we are interested in simulating the system up to the discharge point, and not in subsequent plasma formation (with electron densities of the order of 10^9 cm^{-3} [27]). In the case of the study of plasma, inter-electron effects are extremely important, and the concept of macroparticle facilitates its computation.

As we are not interested in plasma simulation, we can track single electrons, and then obtain a more fine-grain information in the simulation, like the number of collisions of each electron, its MP mode, etc.

PIC codes usually work by integrating a number of differential equations for each electron, thus advancing the time of each electron simultaneously (i.e. using a continuous simulation approach). In our case, in MEST we can use a discrete-event approach, as the trajectory equations can be solve analytically. Note however, that for the case of CEST, we use a similar approach to PIC codes, but still we track single electrons, and not macroparticles. Moreover, we use a hybrid approach by using the Langevin equations for the modelling of the trajectories (where distortion of the electrons due to the gas atoms is represented by the random coefficient), and the collisions relevant for the discharge are represented as discrete events.

With respect to tools, the aforementioned work of [28] is built on top of FEST3D, a microwave circuits design tool. Altogether, the processing follows a batch approach, where results can be inspected only after all the simulations have finished. On the contrary, we offer run-time information while the simulation proceeds, so we can visualize the evolution of the electron population, the origin of each electron in the simulation, the electronic temperature, etc. Other tools, like the Multipactor Calculator [16], are not based on simulation, but implement theoretical models (Hatch and Williams) and offer a number of additional calculations. Our model is not based on the resonant electron theoretical model of Hatch and Williams, but on a SEY model of the material. Interestingly, the results we have obtained through simulation seem to agree with such theory. Recent questions to the Hatch and Williams theory, such as the existence of hybrid modes [14] can also be investigated with our tool, however this is up to future work. See [13] for a review of some simulation tools for MP, all of them implement models following a continuous simulation approach.

8 Conclusions and Future Work

In this paper we have described two software tools (MEST and CEST) for the simulation of different electron discharge processes in waveguides: Multipactor and Corona. Both tools are based on original, novel, microscopic models based on the individual tracking of single electrons. The tools have proven useful from an engineering point of view, for the prediction of the discharge regions ($V - f \times d$ and $V - p$, the Paschen curve) arising with the use of diverse coating materials and the presence of different gases in the device. From a scientific point of view, the graphical output forms provided by the tools allow studying and analyzing the different processes involved in the discharges. In particular, CEST has proved especially useful in the understanding of the processes arising the intermediate pressure range, where electrons are produced both at the walls and due to ionization. The tools where built under a project sponsored by the European Space Agency, and are being successfully used for the prediction of these discharges.

In the future, we will probably improve the tools by adding additional output forms able to analyze further simulation data to allow further verification of theories [9, 14]. More complex RF signals and geometries are under consideration. We are also considering the use of software product-family approaches and generative technologies based on Domain Specific

Languages for the personalization of the interfaces, graphical outputs and simulation models.

References

[1] Birdsall, C. K. 1991. *Particle-in-Cell Charged-Particle Simulations, Plus Monte Carlo Collisions With Neutral Atoms, PIC-MCC.* IEEE Transactions on Plasma Science, Vol **19**(2), pp. 65 – 85.

[2] Brown, S. C. 1994. *Basic data of plasma physics: The fundamental data on electrical discharges in gases.* American Vacuum Society Classics American Institute of Physics, New York.

[3] Catani, J.-P. and Puech, J. 2000. *Microwave breakdown in space RF hardware.* Proc. workshop on Multipactor, RF and DC Corona and passive intermodulation in space RF hardware, pp. 25-30, WPP-178, ESTEC, ESA, Noordwijk, The Netherlands.

[4] Farnsworth, P. T. 1934. *Television by electron image scanning.* Journal Franklin Institute **218**, pp. 411-444.

[5] Fishman, G. S. 2001. *Discrete Event Simulation. Modeling, Programming and Analysis.* Springer Series in Operations Research.

[6] Furman, M. A., Pivi, M. T. 2002. *Probabilistic Model for the Simulation of Secondary Electron Emission.* Physical Review Special Topics - Accelerators and Beams **5**, pp. 124-404.

[7] Gardiner, C. W. 1985. *Handbook of Stochastic Methods for Physics and the Natural Sciences 2nd Edition.* Springer-Verlag, Berlin.

[8] Gilardini, A. 1999. *The radiofrequency breakdown in low pressure argon.* Journal of Physics D: Applied Physics **32**, pp. 1281-1286. IOP.

[9] Hatch, A. J., Williams, H. B. 1954. *The Secondary Electron Resonance of Low-Pressure High-Frequency Gas Breakdown.* Journal of Applied Physics **25**(4), pp. 417-423.

[10] Higham, D. J. 2001. *An Algorithmic Introduction to Numerical Simulation of Stochastic Differential Equations.* SIAM Review **43**(3), pp. 525-546.

[11] Höhn, F., Jacob, W., Beckmann, R., Wilhelm, R. 1997. *The transition of a multipactor to a low-pressure gas discharge.* Physics of Plasmas **4**(4), pp. 940-944.

[12] Kishek, R. A., Lau, Y. Y. 1998. *Multipactor Discharge on a Dielectric.* Physical Review Letters **80**(1), pp. 193-196.

[13] Krawczyk, F. L. 2001. *Status of Multipacting Simulation Capabilities for SCRF Applications.* Proc. of the 10th Workshop on RF Superconductivity, Tsukuba, Japan.

[14] Kryazev, A., Buyanova, M., Semenov, V., Anderson, D., Lisak, M., Puech, J., Lapierre, L., Sombrin, J. 2002. *Hybrid Resonant Modes of Two-Sided Multipactor and Transition to the Polyphase Regime.* Physics of Plasmas **9**(11), pp. 4736-4743.

[15] de Lara, J., Pérez, F., Alfonseca, M., Galán, L., Montero, I., Román, E., Raboso, D. 2006. *Multipactor Prediction for On-Board Spacecraft RF Equipment with the MEST Software Tool*. IEEE Transactions on Plasma Science **34**(2), pp. 476- 484.

[16] Multipactor Calculator (by Strijk, S.J.G.) home page at: http://multipactor.esa.int/

[17] Pérez, A. M., Tienda, C., Vicente, C. P., Sánchez, J. F., Coves, A., Torregrosa, G., San Blas, A. A., Gimeno, B., Boria, V. E. 2005. *MULTICOAX: A Software Tool for Predicting Multipactor RF Breakdown Threshold in Coaxial and Circular Waveguides*. Proc. 5th International Workshop on Multipactor, Corona and Passive Intermodulation in Space RF Hardware (MULCOPIM), ESA/ESTEC, Noordwijk, The Netherlands, pp.27-34.

[18] Raizer, Y. P. 1991. *Gas discharge physics*. Springer Verlag, Berlin.

[19] K. U. Riemann. 1992. *Theory of electron distribution function in a Lorentz gas at high* E/n_o. Phys. Rev. A **46**, (8) pp. 4717-4728.

[20] Riyopoulos, S. 2004. *Collisional multipactor inside ambient gas*. Physics of Plasmas **11**(5), pp. 2036-2045.

[21] Semenov, V., Kryazhev, A., Anderson D., Lisak, M. 2001. *Multipactor suppression in amplitude modulated radio frequency fields*. Physics of Plasmas **8**(11), pp. 5034-5039.

[22] Somersalo, E., Yla-Oijala, P., Proch, D. 1995. *Analysis of multipacting in coaxial lines*. Proc. Particle Accelerator Conference **3**, pp. 1500-1502.

[23] L. Stenflo. 1966. *Runaway in weakly ionized plasmas*. J. Nuclear Energy, Part C Plasma Phys. **8**, pp. 665-673.

[24] Udiljack, R., Anderson, D., Lisak, M., Semenov, V.E., Puech, J. 2003. *Multipactor in low pressure gas*. Physics of Plasmas **10**(10), pp. 4105-4111.

[25] Udiljack, R., Anderson, D., Lisak, M., Semenov, V.E., Puech, J. 2004. *Improved multipactor in low pressure gas*. Physics of Plasmas **11**(11), pp. 5022-5031.

[26] Vaugham, J. R. M. 1988. *Multipactor*. IEEE Transaction on Electron Devices **35**(7), pp. 1172-1180.

[27] Vender, D., Smith, H. B., Boswell, R. W. 1996. *Simulations of multipactor-assisted breakdown in radio frequency plasmas* Journal of Applied Physics **80**(8), pp. 4292-4298.

[28] Vicente, C., Mattes, M., Wolk, D., Hartnagel, H.L., Mosig, J.R., Raboso, D. 2005. *FEST3D - A simulation tool for corona prediction*. Proc. 5th International Workshop on Multipactor, Corona and Passive Intermodulation in Space RF Hardware (MULCOPIM 2005), ESA/ESTEC, Noordwijk, The Netherlands, pp. 227-233.

[29] Woode A., and Petit, J. 1989. *Diagnostic Investigations into the Multipactor Effect, Susceptibility Zone Measurements and Parameters Affecting a Discharge*. ESTEC Working Paper No. 1556. ESTEC, Noordwijk.

[30] A. G. Zhidkov. 1998. *Simulation of electron runaway in a plasma by Langevin equation.* Phys. Plasmas, **5**, (2), pp. 385-389.